Chapter – 2

Materials & Methods

2.1. Precursor oxides

The individual metal oxides were procured in powder form with particle size ranging from 40-50 μm (mesh size) from either Alfa Aesar or Sigma Aldrich. The purity of the individual oxides exceeds 99.5 at% for most while it is more than 99.9 % for some of them. An exhaustive list of the precursor oxides, their purity, ionic radii at specific coordination environment along with their preferred crystal structure is given in Table 2.1. The individual oxides were so chosen to understand entropic stabilization in quinary multicomponent oxides through systematic partial substitution. Since HEOs/ESOs show excellent functional properties in most cases than not, it is worth examining the microstructural evolution and phase stability in such chemically complex systems.

2.2. Solid-state synthesis

There are several ways of synthesizing materials through powder metallurgy route classified broadly under two categories i.e. top-down approach and bottom-up approach [1]. Among them, there could be many further classifications based on length-scale (micron, sub-micron, nano), morphology control, processing environment and so on [1-3]. For the research work pertaining to this thesis, solid-state route of top-down approach has been selected mostly because of the relative ease of handling raw materials coupled with high success rate of synthesis. The purity of precursor oxides procured, their molecular weights, ionic radii at specific coordination environment (six-fold coordination unless otherwise mentioned) and their preferred crystal structures have been listed in Table 2.1 [4,5]. The precursor powders have been weighed in equimolar proportions, mixed thoroughly in a mortar and pestle before uniaxially compacting the mix in a hydraulic press under 4T load. The green compacted pellets of ~12 mm diameter and ~4-5 mm thickness were subjected to various sintering heat treatment schedules (Figure 2.1a). Green

compacted pellets of each and every composition have been stacked vertically inside a platinum crucible with the platinum lid on, and the sintered pellets from the centre of the stacks were taken for further examination. This ensured uniform sintering with minimal contamination. The sintering process has been carried out in a high-temperature tube furnace with $MoSi_2$ heating filament and in air atmosphere. The detailed heat treatment cycles are schematically shown in Figure 2.1a. In another set of samples, ball-milling has been adopted to examine the effect of high strain rate processing on phase evolution apart from uniform mixing. High-energy ball-milling was carried out in a Retsch PM-400 planetary mill operating at 200 rpm in dry atmosphere (Figure 2.1b). Zirconia vial and zirconia balls were used for milling, with ball to powder ratio maintained at 10:1. The milling has been carried out for 1 minute at a stretch followed by 30 seconds of idle time which was again followed by a minute of milling and so on. This was carefully controlled so that the local rise in temperature upon continuous ball milling does not induce dynamic recrystallization [6]. Samples were taken out at regular intervals of ball-milling to understand the phase evolution and it was continued for a maximum of 40 h.

Table 2.1: Table of precursor oxides depicting their purity, molecular weight, ionic radii and preferred crystal structure with space group notation and Pearson symbol.

	CaO	Co(II,III)O	Cr(III)O	CuO	Fe(III)O	MgO	Mn(III)O	NiO	ZnO
Purity (%)	99.95	99.8	99.9	99.9	99.8	99.98	99.8	99.9	99.95
Mol. Wt. (a.m.u.)	56.07	240.795	151.989	79.54	159.687	40.304	157.873	74.69	81.37
Ionic Radii (Å)	1 (6)- 1.34 (12)	0.75 (+2) 0.55 (+3)	0.62	0.77 (+1) 0.73 (+2)	0.78 (+2) 0.65 (+3)	0.72 (6) 0.57 (4)	0.72	0.69	0.74
Preferred Crystal structure	Rocksalt Fm-3m, cF8	Rocksalt/Spinel Fm-3m, cF8 / Fd-3m, cF56	Corrundum R-3c hR10	Tenorite C2/c mC8	Corrundum R-3c hR10	Rocksalt Fm-3m cF8	Bixbyite Ia-3, cI80 / Spinel, cF56	Rocksalt Fm-3m cF8	Wurtzite/Zinc Blende $P6_3mc$/F-43m hP4/cF8

During high-energy ball-milling, the powder particles undergo a process of cold welding, repeated fracture and rewelding. For this reason, such processes were coined as Mechanical Alloying (MA) techniques by the International Nickel (INCO) company during the early 1960's. The recognition of MA, from a mixing tool to a potential non-equilibrium

processing technique took place during the early 1980's when it was observed that Ni-Nb system and Y-Co intermetallic compound formed amorphous phase. Further investigations employing MA routes produced a variety of stable and metastable phases including supersaturated solid-solutions, crystalline and quasicrystalline intermediate phases along with amorphous alloys [6]. The use of high-energy ball-milling in the course of this research has been primarily to refine particle size and yield homogeneous inter-mixing of multiple constituent oxides. However, it does bring out another competing phenomenon which will be elucidated in Chapter 5 of the thesis.

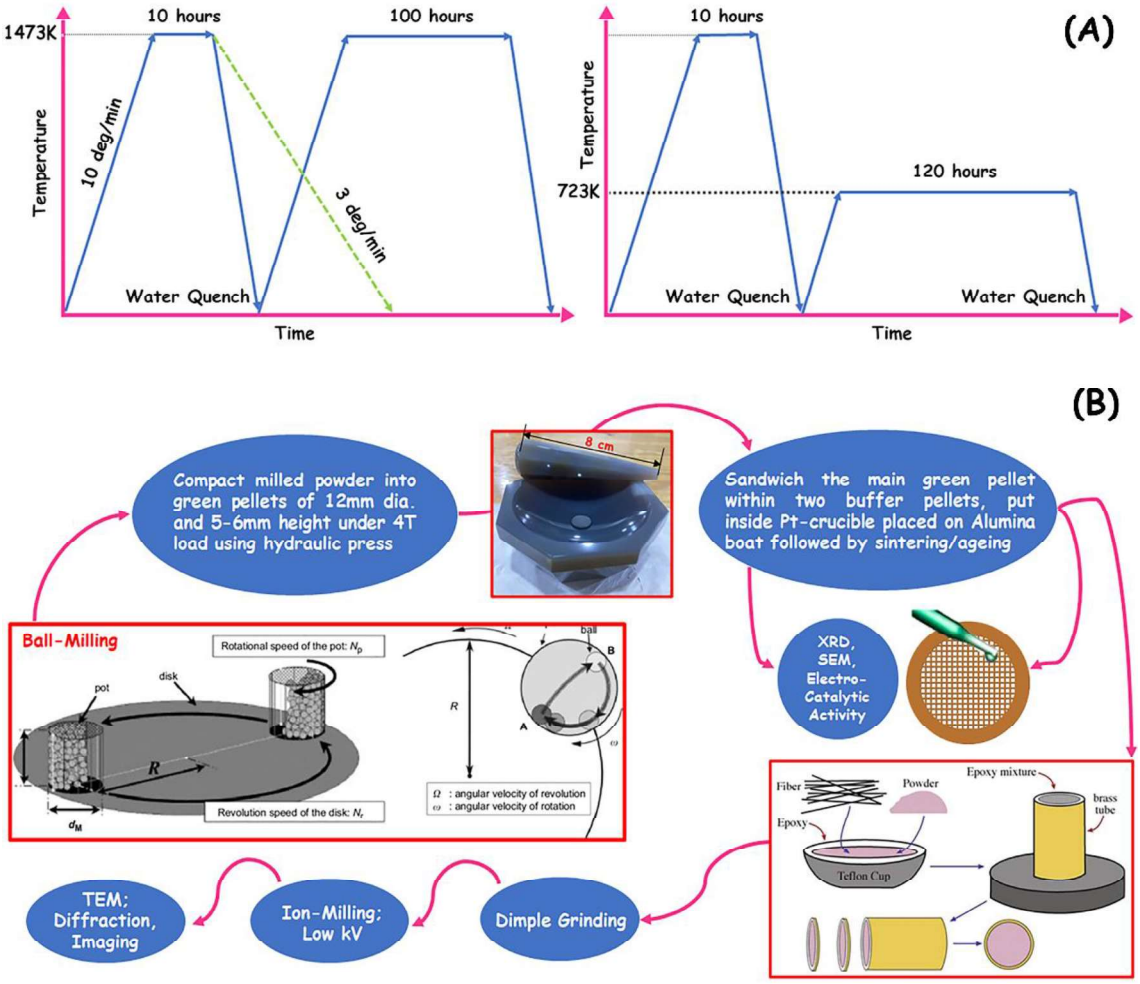

Figure 2.1: (a) Time-temperature diagram showing sintering of consolidated green pellets under various heat treatment schedules, which has been implemented for various multi-cationic compositions throughout the thesis. (b) Schematic showing mixing of powders in definite proportion, their consolidation followed by meticulous sample preparation for extensive characterization.

2.3. X-ray diffraction (XRD)

X-rays were discovered by Roentgen in 1895 after his persistent experimentation with Lenard's tube on C_4BaN_4Pt sample and was named so because of their unknown nature at the time [7]. Little did the German physicist know that this discovery would spark the scientific revolution of the late 19^{th} and early 20^{th} century. Radiography was shortly initiated by physicians and medical personnels to investigate internal organs of patients without precise knowledge of the radiation being used [8,9]. X-rays were subsequently treated as waves in the lines of Huygen's principles and Young's double-slit experiments. Couple of years after its discovery, Thomson demonstrated that X-rays could ionize gas and this led to the discovery of electrons in 1897. However, the most profound work arising out of constant curiosity regarding the very nature of X-rays led Becquerel to accidentally discover radioactivity, before M. Curie and P. Curie advanced our understanding of the subject further by leaps and bounds. Both these imperceptible yet powerful rays imparted new tools to probe almost anything and everything around us while elegantly bringing out the deficiencies in our own senses. Soon, groundbreaking work by Einstein yet again reclaimed the particle nature of X-rays by demonstrating the photoelectric effect in 1905. However, it was not until 1912 that the exact nature of X-rays was established. Due to pioneering works of Ewald and Von Laue, the phenomenon of X-ray diffraction by crystals was discovered [10]. This discovery at one hand proved the wave nature of X-rays and on the other hand provided a new method for investigating the fine structure of matter. It is now understood that X-rays are electromagnetic (EM) radiation of the same nature as light, but of much shorter wavelength. Electromagnetic radiation according to classical mechanics is treated as a wave while it is treated as a stream of particles (quanta or photons) according to quantum mechanics, an extension to the revolutionary concepts put forth by Bohr, de Broglie, Heisenberg, Schrodinger among others. A schematic of the entire EM

spectrum is given in Figure 2.2 with range of energy, frequency and wavelength highlighted on top and bottom. Von Laue worked out the mathematics of diffraction by x-rays from a periodic arrangement of atoms in a 3D crystal which opened up two broad fields i.e. crystal structure determination and spectroscopy related measurement and quantification. The later was dealt by Friedrich and Knipping while W.L. Bragg and W.H. Bragg tackled the first problem and came up with the celebrated Braggs law of crystal diffraction [11].

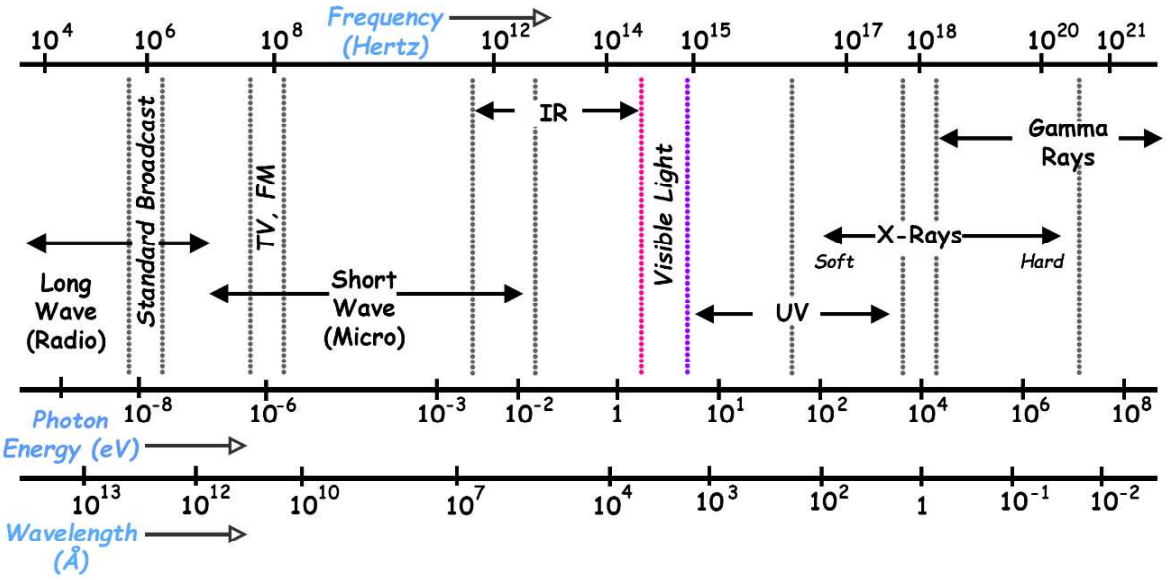

Figure 2.2: Schematic of the electromagnetic (EM) spectrum.

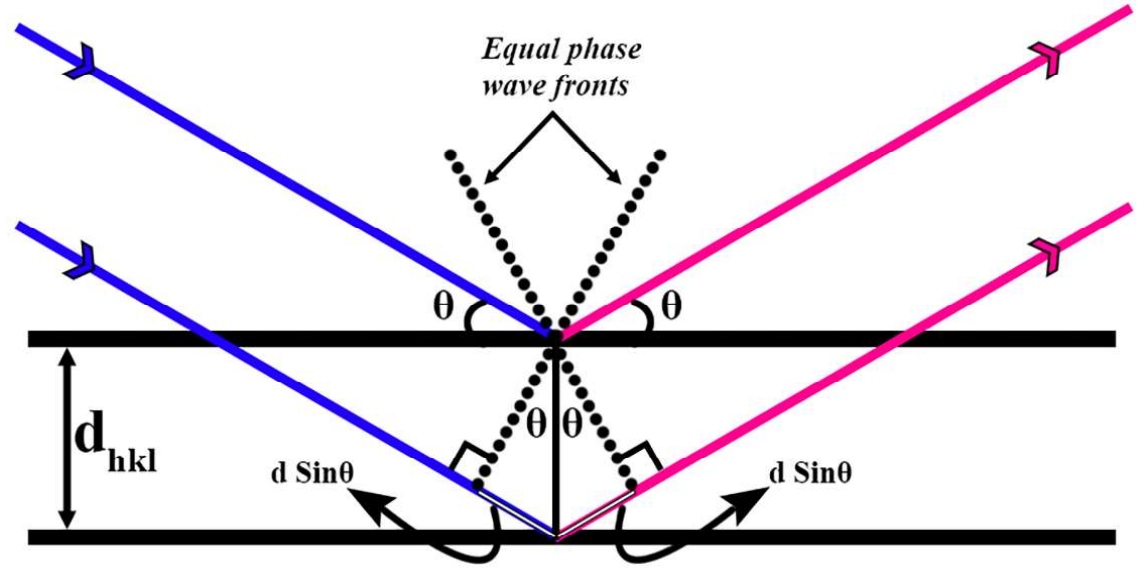

Figure 2.3: Schematic of the Real-space formulation of Braggs law for X-ray diffraction.

XRD experiments for probing internal structure of materials was understood to be essentially reinforced coherent scattering from periodic lattice planes decorated by crystal motifs. Braggs law dictates that the path difference between the top and bottom layer of the same family of crystallographic planes must equal one wavelength for constructive interference, and hence strong diffraction to occur (Figure 2.3). Therefore,

$$\mathbf{d_{hkl}\ sin\theta + d_{hkl}\ sin\theta = \lambda} \qquad \textbf{(i)}$$

$$\mathbf{\lambda = 2d_{hkl}\ sin\theta} \qquad \textbf{(ii)}$$

It is frequently encountered that the LHS of the equation is multiplied by an integer "n" since this also provides prerequisite condition for constructive interference. However, this convention can be circumvented by dividing d_{hkl} by n which gives a more realistic picture of constructive interference from the n^{th} order diffracting planes. It then becomes possible with the help of this simple yet powerful equation to calculate interplanar spacings from a set of diffracting planes and work out the crystal structure of unknown materials. Interestingly, the determination of crystal structures helped to shed light on the nature of chemical bonds in a material when Bragg and Bragg examined NaCl to dismiss the idea of NaCl molecules in favour of positive and negative ions bound by electrostatic forces in ionic bonding [12]. X-ray and matter interaction soon opened up a field of science on its own and X-ray crystallography was born (Figure 2.4). Although the generation of x-rays has electronic origins, it can effectively be used to probe the crystal structure of metals and its alloys, ceramics and its compounds to glasses, amorphous materials and quasicrystals. Depending on the input stimulus and properties of the material to be investigated, several signals carrying a wealth of information may be retrieved upon x-ray and matter interaction. The knocking-off of an electron from the innermost shell of an atom is known to produce characteristic excitation lines (characteristic x-rays) and the filling up process from higher

order shells may give rise to secondary x-rays, fluorescent radiation or Auger electrons [8]. A schematic representing the major signals produced in events of strong x-ray and matter interaction is given in Figure 2.4. Although the very definition of x-ray diffraction demands coherent elastic scattering process, however that is an idealised situation and deviation from ideality is unavoidable. Generally, the signals can broadly be classified under four categories: *elastic coherent*, *inelastic coherent*, *elastic incoherent* and *inelastic incoherent*. Usually, the spectroscopic principles rely on incoherent and inelastic scattering while neutron scattering relies on inelastic coherent scattering [9].

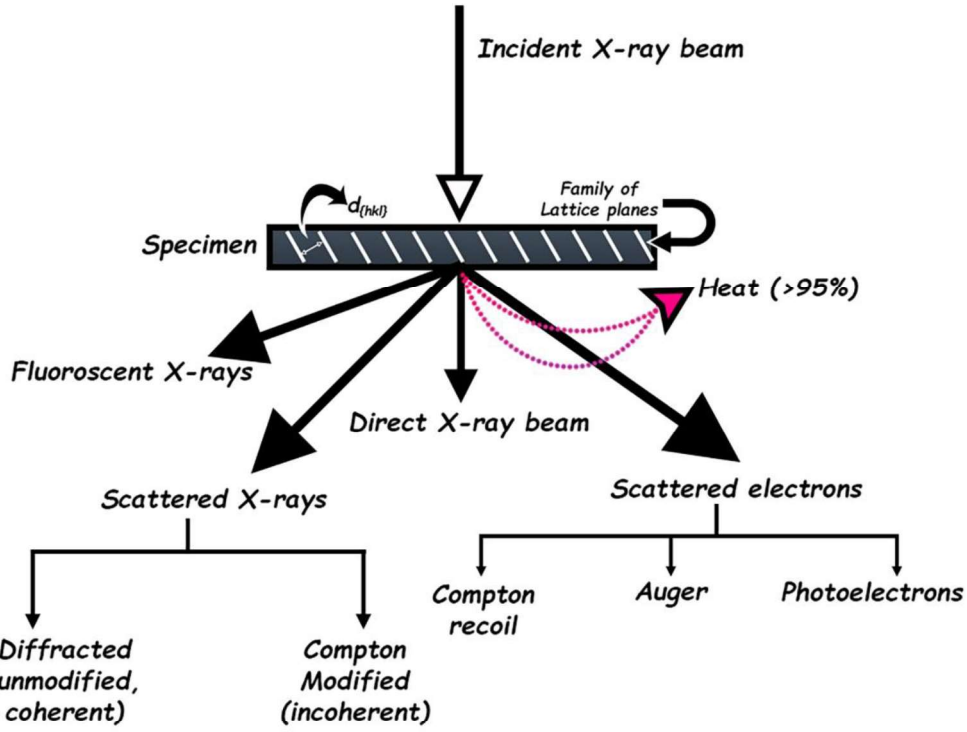

Figure 2.4: Schematic representing various kinds of signal generation on interaction between x-ray and matter.

Determination of crystal structure relies on the fact that the diffraction signature (pattern) is nothing but a Fourier transform of the atomic scattering function distribution of a material [9]. This translates to intensity as a function of 2θ in a systematic pattern of delta functions according to the extinction conditions of a particular type of crystal structure. However, the

finite width in the peaks and its shape evolution is indicative of the contributions from grain/particle size distribution and lattice strain in polycrystalline materials [8]. Further information regarding presence of second phases may be found out by deconvolution of peaks. Ratio of peak intensities is another useful parameter for structural refinement while normalised peak ratios provide approximate phase fractions in multi-phase materials. Thomson scattering on one hand is responsible for the sharp signature peaks while Compton scattering on the other, discovered in 1923, was helpful in demonstrating the particle nature of light after the photoelectric effect [13]. However, it proved to be a nuisance in diffraction work as it contributes to the background noise in diffraction patterns owing to the incoherent and inelastic nature of the radiation. It turns out that since the total integrated intensity of peaks are inversely proportional to both the mass absorption coefficient as well as the cell volume squared, large lattice parameter phase(s) of high molecular weight metallic compounds/ceramics contribute to enhanced Compton modified background than their metallic alloys counterpart. Details of sample preparation, make and model of diffractometers used along with its process parameters are reported in the 'materials and methods' section of each chapter.

2.4. Transmission electron microscopy (TEM)

On one hand XRD was providing indirect signatures so as to decode the crystal structure of a material while optical microscopy (VLM) on the other was able to provide microstructural information, however, the spatial resolution was restricted to the micron or at-best the sub-micron range. In extraordinary circumstances, Ruska and Knoll came up with first prototype of a working TEM during early 1940's, surpassing the resolution limit of visible light [14]. It took almost two decades after their invention, before the first ever commercial TEM was launched, due to the robust engineering challenges associated in assembling such electron microscopes. It has been a journey of no looking back since then,

with continuous and rapid improvement in vacuum technology, high voltage technology, electronics, automation and manufacturing of detectors, electromagnetic lenses along with their aberration correction [15-17]. The resolution limit has gone down from sub-micron to nano to sub-nano and even sub-angstrom length scales with scope for further improvement. Since a TEM image projects the 3D internal structure of materials in a 2D plane at unprecedented resolution and magnification, the human brain generally fails to fathom the richness of information by just looking at it. The humongous contribution by electron microscopy experimentalists and theoreticians alike in the last several decades towards the advancement of the field is filled with richness and its comprehensive accord is beyond the scope of the thesis [18].

Various contrast forming mechanisms occupy the heart of TEM imaging. They may be broadly classified as; (1) Amplitude contrast (special case is diffraction contrast under 2-beam geometry), (2) Z-contrast and (3) Phase contrast [16]. The dynamic coupling of direct and diffracted beams produces diffraction contrast and can be appreciated better with the help of Howie-Whelan equations [15-18]. These simultaneous partial differential equations explain the origin of bend contours and thickness fringes as important imaging artifacts, along with contrast mechanisms arising from various defect structures. The TEM primarily is operated under two modes; one is the conventional parallel illumination setup (CTEM) with activated pre- and post-specimen lenses and the other is the scanning transmission (STEM) mode with only pre-specimen lens and scan coils activated. Theorem of reciprocity along with advanced beam and lens correction has advanced Scanning-TEM techniques like STEM-HAADF and STEM-EDS/EELS under convergent electron probe setup. There are several advantages as well as disadvantages of using parallel or convergent mode for TEM observations, although the nature of the material problem under investigation dictates the reliance of the technique to be used.

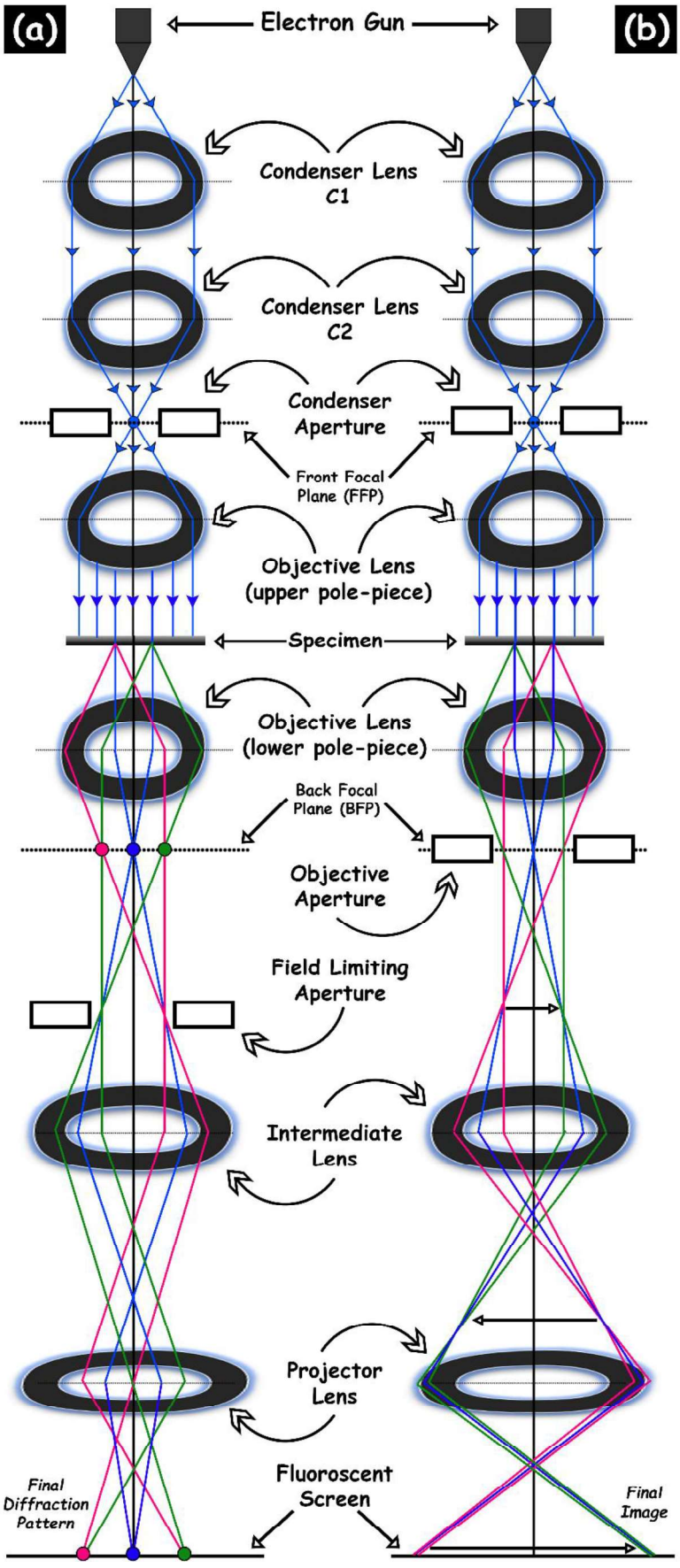

Figure 2.5: Schematic of the TEM under (a) diffraction and (b) imaging mode.

A detailed schematic of TEM under diffraction and imaging mode is given in Figure 2.5. Apart from imaging nanostructures and atom columns, the TEM is a very powerful tool pertaining to single crystal diffraction work. In this context, Bragg's law with respect to real-space formalism is perfectly corroborated with Laue and Ewald's treatment of the reciprocal-space. The symmetry considerations for diffraction geometry demands that the unit vector normal to the diffracting planes be parallel with the diffraction vector i.e.

$\mathbf{\Delta k} \parallel \mathbf{n}$.

The ray diagram of a possible diffraction event in the reciprocal-space formalism is schematically shown in Figure 2.6. The Laue condition of diffraction is satisfied when the diffraction vector ($\mathbf{\Delta k}$) equals the reciprocal lattice vector ($\mathbf{g}$). Under this special condition, the coefficients of the reciprocal lattice vectors take on special integer values corresponding to the miller indices of the allowed set of planes. This results in:

$$\mathbf{\Delta k \cdot a = h;\ \Delta k \cdot b = k;\ \Delta k \cdot c = l} \qquad \textbf{(iii)}$$

Where a, b and c are lattice vectors. Since TEM sample geometry is restricted to a few mm in length and breadth, but only a few tens of nm in its thickness, it lifts off the restriction on the third Laue condition (unlike XRD) and allows for diffraction spots from higher order Laue zones to be simultaneously present in the pattern. This is further facilitated by the fact that the Ewald sphere cuts the reciprocal space with almost zero curvature since radius of the sphere is far greater than the reciprocal lattice vectors and thus allows for collection of data from very small volumes. Moreover, the formation of 1-D rail-rods in place of otherwise 0-D points arising out of the thin foil effect (thickness of electron transparent samples are infinitesimally smaller compared to their surface dimensions) also facilitates much stronger electron-matter interactions at non-exact Bragg angles than x-ray and matter [16].

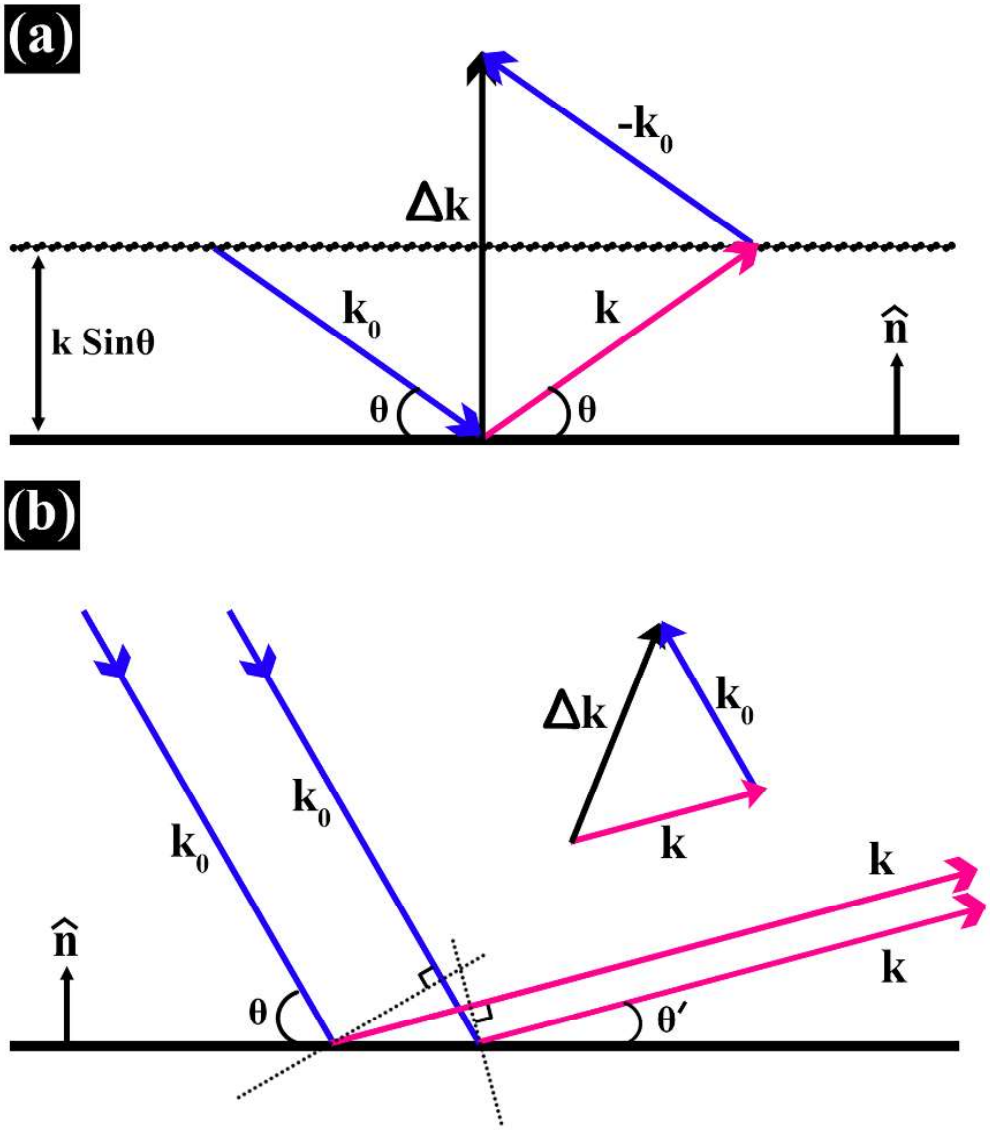

Figure 2.6: Schematic representing the diffraction setup in reciprocal space for (a) proper and (b) improper geometry.

2.5. Scanning electron microscopy (SEM)

Modern science is heavily reliant on microscopy as seeing is believing. The invention of the TEM quickly saw its upgradation to a STEM by retrofitting a pair of scan coils, which was then used to take the first STEM micrograph of a ZnO crystal at 23 kV at ~50 nm resolution [19]. However, the first demonstration of the capabilities of a Scanning Electron Microscope (SEM) for surface characterization came couple of decades later from Smith and Oatley [20]. It was Oatley's students who made incremental progress to the optical

setup and the SEM started to be commercialised with the advent of digital electronics [21,22]. There are no post-specimen lenses in an SEM, since a fine electron-probe falls on the surface of the specimen to scan it in raster manner and generate various signals that are then captured by dedicated detectors. The specimen chamber in an SEM can accommodate multiple samples mounted on metallic stubs. Electrically conducting samples are readily imaged and examined under the SEM, however, gold/carbon coating is required for insulators. Imaging and spectroscopy are the two most commonly used modes in a SEM. However, it also has the capability of performing electron backscattered diffraction (EBSD) which can map the relative orientation of grains or microstructural features [22].

The primary contrast forming mechanism in SEM images include topographical contrast in secondary electron (SE) images and atomic number contrast in backscattered electron (BSE) images. The most pronounced advantage of an SEM as an investigation tool arises from its high depth of field. It may be defined as the ability of the system to image features at differential heights from the surface with negligible loss of resolution. This makes the SEM an ideal choice for non-destructive testing (NDT) and fracture surface analysis [21]. Apart from several contrast mechanisms, lens aberrations significantly affect the quality of the final image. Cranking up the magnification without correcting for the lens defects systematically leads to aberrations in the optical system to blow up further. A schematic representing the major lens defect is presented in Figure 2.8. Since electrons interact much more strongly with matter than the strongest of x-rays (low wavelength high energy), the penetration depth of electrons is usually much smaller. Auger electrons are ejected from a depth of ~ 10 Å from the surface followed by secondary electrons which come out from ~ 50-500 Å while back-scattered electrons and x-rays are emitted from further depths, often restricting the total interaction volume to few tens of a nm in thickness. The types of signals expected from electron-matter interaction is given in Figure 2.7.

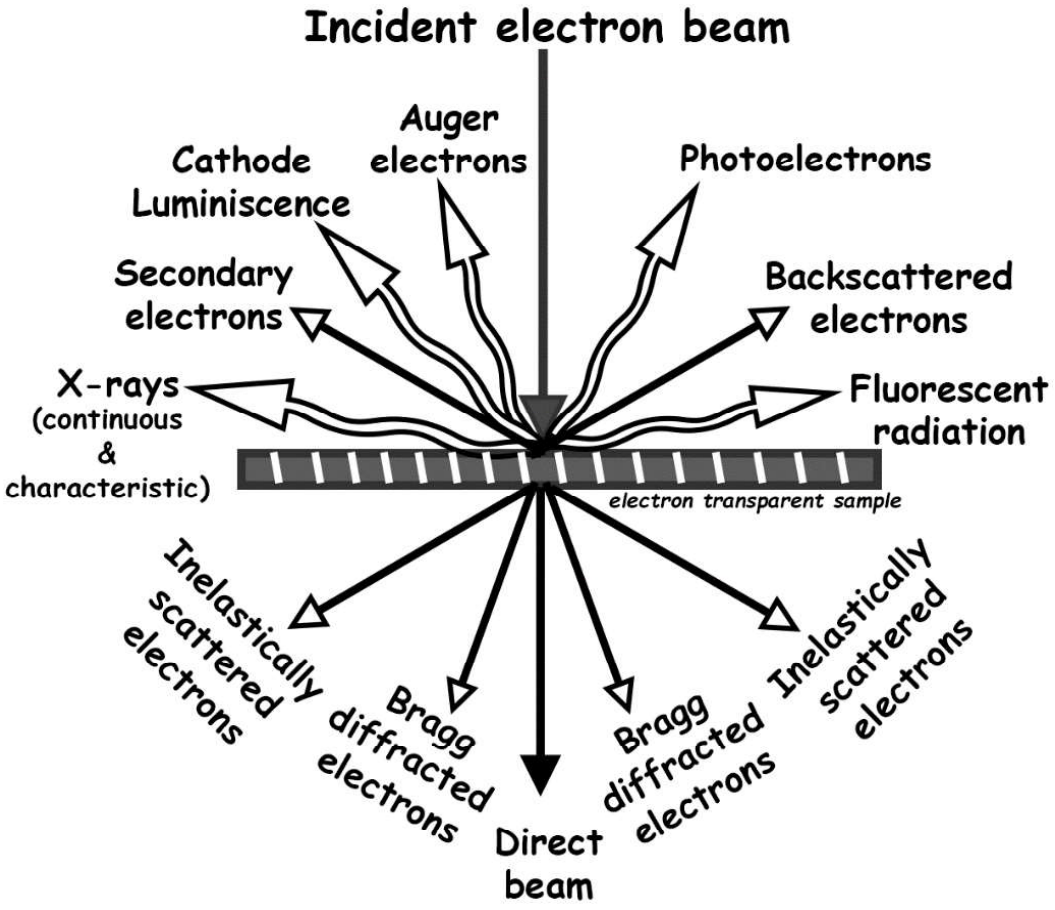

Figure 2.7: Schematic of the various kinds of signals that are produced from typical interactions between electron and matter.

The scattering cross-section at constant energy varies with "Z^2" (atomic number) and the probability of scattering through a given angle varies as "$(Z/E)^2$". It follows from calculations of Murata et al. that the mean free path between scattering events at 30 keV decreases with increasing atomic number from ~528 Å for Al to ~131 Å for Cu and ~50 Å for Au. Since the probability of scattering is low and the mean free path is large for low atomic number elements, there is not much scattering near the surface of the specimen as the electron enters. As the energy of the electrons decreases during passage through the sample, the number of scattering event increases and a state of complete diffusion of electron trajectories can be expected. This results in a pear-shaped interaction volume when

any specimen is examined under the SEM as has been corroborated with Monte-Carlo simulations [22].

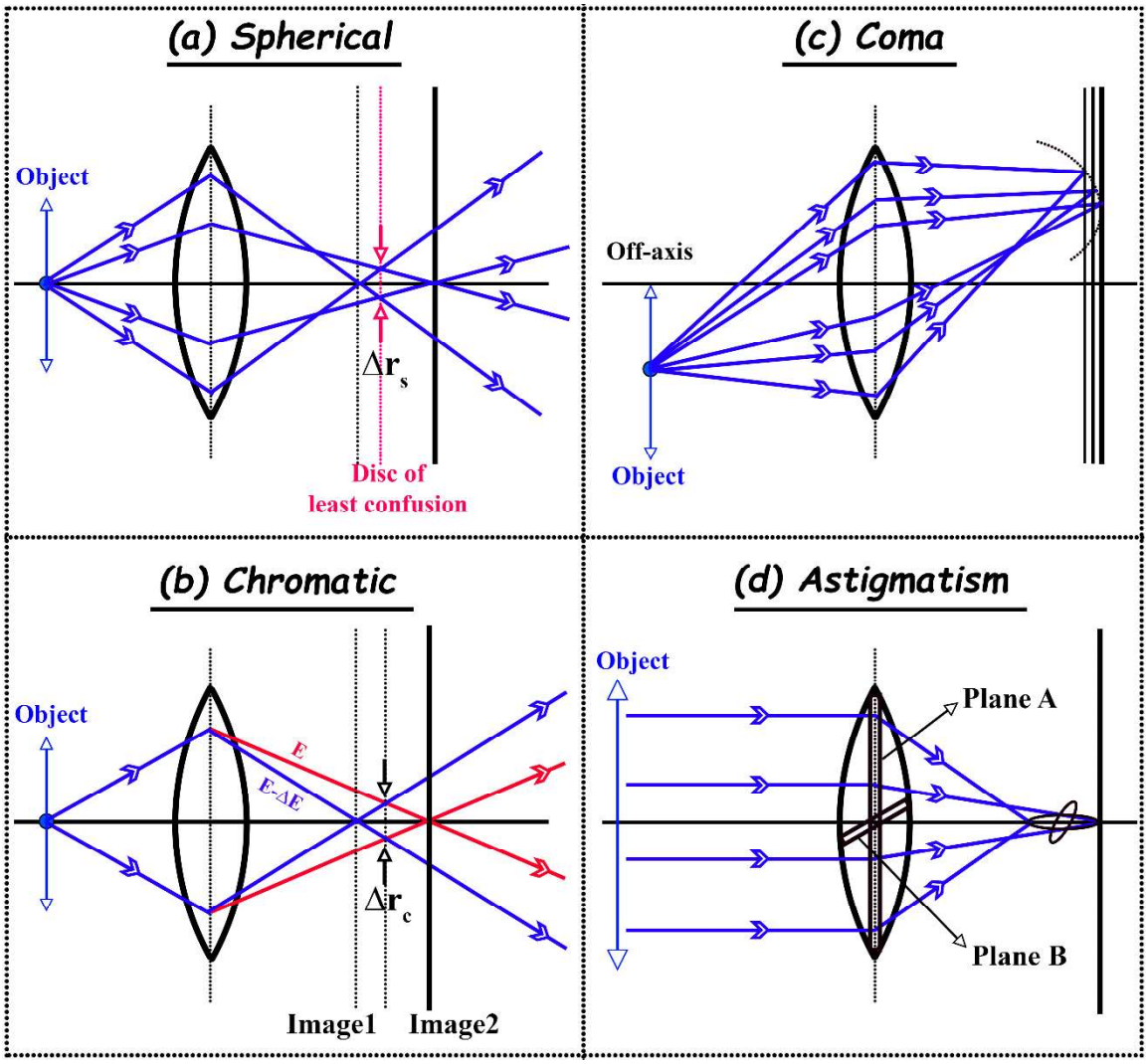

Figure 2.8: Schematic diagram of the four primary electromagnetic lens aberrations.

2.6. Structure Modelling and Simulation

Analysis of results (top-down) pertaining to diffraction or imaging using electrons and even x-rays often require complementary approaches (bottom-up) to arrive at satisfactory conclusions. In this regard, modelling and simulation provides a powerful tool if used cautiously. The research work undertaken throughout the thesis combines experimental evidences with structural modelling and simulation of diffraction patterns. For real-space

3-D structure and interfaces, VESTA^{TM} software has been extensively used. Pearsons's handbook of crystallographic data was referred for the Wyckoff positions of ions in the multicomponent oxides [23]. The anticipated presence of complete disorder in entropy stabilized oxides may be treated with idealized Wyckoff positions, whereas formation of two- or multi-phase with probable short-range order and defect structure can make selection of ionic positions quite complicated. Apart from crystal and interface structures, diffraction signature from x-ray and matter interaction has been simulated through indigenously developed code using MATLAB^{TM}. It uses the combined equation accounting for atomic scattering factor, multiplicity factor, polarization factor, temperature and absorption factor to compute the total integrated intensity of x-ray peaks. Furthermore, JEMS^{TM} software was used extensively for generating standard zone-axis electron diffraction patterns and stereographic projections.

2.7. Electrocatalysis

Production of hydrogen through water electrolysis has emerged as the new energy currency owing to its high energy density and zero carbon emission. However, efficient and clean hydrogen production is dependent on the ease of oxygen production as one half of redox reaction, which is highly energy consuming and rate limiting. Therefore, it becomes essential to develop efficient electrocatalysts for enhancing the efficiency of the oxygen evolution reaction (OER) [24-26].

Electrocatalytic activity for efficient catalysis in water-splitting experiments were carried out on an Electrochemical and Corrosion Studio using the CORRTEST software. A three-electrode setup with glassy carbon as working electrode, Ag/AgCl as reference electrode and carbon black as counter electrode all dipped in an 1M KOH solution as electrolyte was used. The glassy carbon electrode was cleaned thoroughly in a slurry of high purity alumina

before “ink” of each composition was drop-cast onto the inverted tail of the glassy carbon electrode (0.071 cm^2 surface area). For preparing the ink, thin slices were cut from the sintered pellets of various compositions and it was ground into powder by mortar and pestle after which 1 mg of the specimen powder was mixed with 10 µL of 5wt% Nafion solution and 350 µL of ethanol in a vial. The vial was then ultrasonicated for sufficient time before ~ 7 µL of the ink was pipetted out on to the glassy carbon electrode. After the setup was complete, linear sweep voltammetry (LSV), cyclic voltammetry (CV) and electron impedance spectroscopy (EIS) was carried out multiple times on each of the compositions for reproducibility of results. Overpotential plots along with Taffel slopes have been computed for each of the multicomponent oxide compositions and the results have been rationaled with respect to the crystal structure, chemical modulation and phase-fractions.

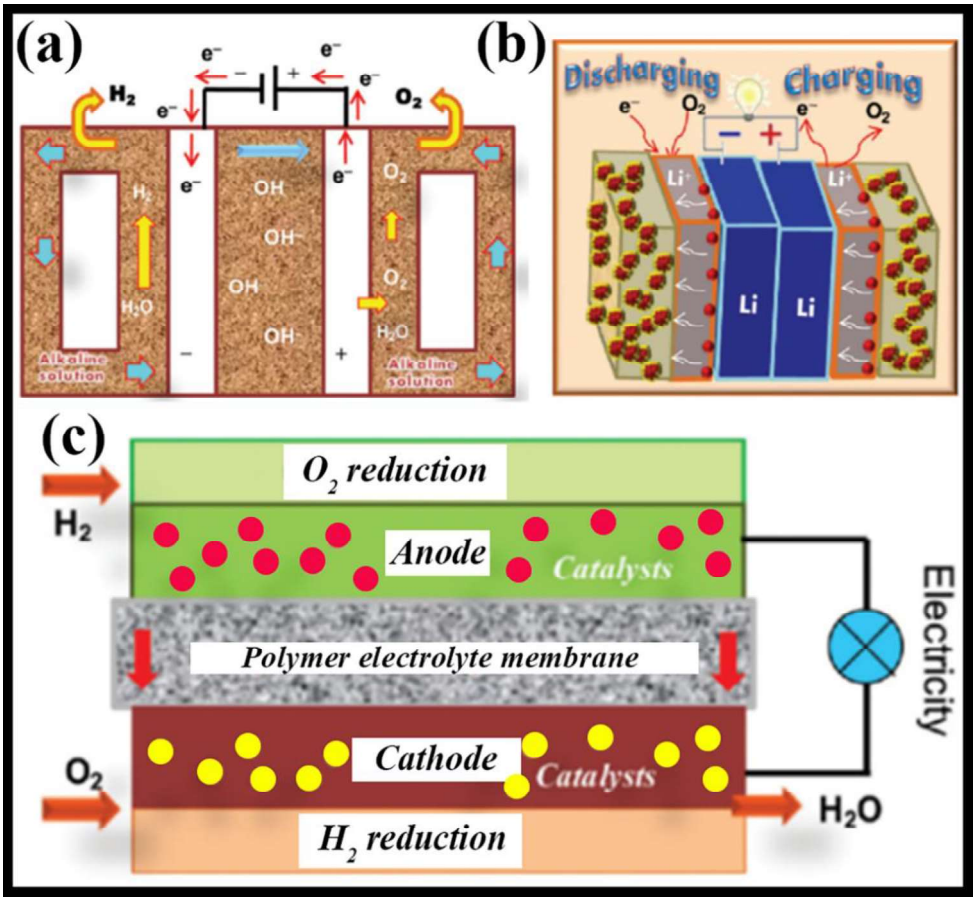

Figure 2.9: Schematic representation of (a) Electrochemical Fuel cell (b) Li-ion battery and (c) Electrocatalysis for water-splitting experimental setup [24,25].

2.8. Reference

1. K. V. Mahesh, S. K. Singh, M. Gulati, A comparative study of top-down and bottom-up approaches for the preparation of nanosuspensions of glipizide, Powder Technology, 2014, Vol. 256, 436-449.
2. B. L. Musico, D. Gilbert, T. Z. Ward, K. Page, E. George, J. Yan, D. Mandrus, V. Keppens, The emergent field of high entropy oxides: Design, prospects, challenges and opportunities for tailoring material properties, APL Mater., 2020, Vol. 8, 040912 (17 pages)
3. L. Lin, K. Wang, R. Azmi, J. Wang, A. Sarkar, M. Botros, S. Najib, Y. Cui, D. Stenzel, P. A. Sukkurji, Q. Wang, H. Hahn, S. Schweidler, B. Breitung, Mechanochemical synthesis: route to novel rock salt structured high-entropy oxides and oxyfluorides, 2020, Vol. 55, 16879-16889.
4. C. B. Carter, M. G. Norton, Ceramic Materials Science and Engineering, Springer Nature, USA, 2013, Edition 2, XXXIII (766 pages)
5. Y. M. Chiang, D. P. Birnie, W. D. Kingery, Physical Ceramics Principles for Ceramic Science and Engineering, John Wiley & Sons Inc., USA, 1997 (542 pages)
6. C. Suryanarayana, Mechanical alloying and milling, Progress in Materials Science, 46, 2001, 1-184
7. M. M. Woolfson, An Introduction to X-ray Crystallography, Cambridge Universty press, UK, Edition 2, 1997 (414 pages)
8. B. D. Cullity, Elements of X-ray Diffraction, Addison-Wesley Publishing Company Inc., USA, Editon 2, 1978 (569 pages)
9. C. Suryanarayana, M. G. Norton, X-ray Diffraction A Practical Approach, Springer Science plus Business Media LLC, USA, 1998 (275 pages)

10. M. Eckert, Max Von Laue and the discovery of x-ray diffraction in 1912: Then and now, Ann. Phys. (Berlin), 524, No. 5, 2012, A83-85
11. W. L. Bragg, The analysis of Crystals by the X-ray Spectrometer, Proceedings of the Royal Society A, 1914, Vol. 89, Issue 613, 469-489
12. W. L. Bragg, The structure of some crystals as indicated by their diffraction of X-rays, Proceedings of the Royal Society A, 1913, Vol. 89, Issue 610 (31 pages)
13. P. Eisenberger, P. M. Platzman, Compton scattering of X-rays from bound electrons, Physical Review A, Vol. 2 (2), 415-423
14. E. Ruska, The development of the electron microscope and of electron microscopy, Reviews of Modern Physics, 1987, Vol. 59 (3) (24 pages)
15. B. Fultz, J. Howe, Transmission Electron Microscopy and Diffractometry of Materials, Springer, Verlag, Berlin, Heidelberg, Edition 3, 2008 (771 pages)
16. D. B. Williams, C. B. Carter, Transmission Electron Microscopy: A Text Book for Materials Science, Springer, New York, USA, Edition 2, 2009, Vol. I-IV (779 pages)
17. J. W. Edington, Practical Electron Microscopy in Materials Science, The McMillan Press, London and Eindhoven, 1974, Vol. I-V (558 pages)
18. Z. L. Wang, New developments in Transmission Electron Microscopy for Nanotechnology, Adv. Mater., 2003, Vol. 15 (18), 1497-1514
19. E. Olsson, L. K. L. Falk, G. L. Dunlop, R. Osterlund, The microstructure of a ZnO varistor material, J. Mat. Sci., 1985, Vol. 20, 4091-98
20. C. W. Oatley, The early history of the scanning electron microscope, J. Appl. Phys., 1982, Vol. 53 (2) (14 pages)
21. N. Tanaka, Scanning Transmission Electron Microscopy of Nanomaterials: Basics of imaging and analysis, Imperial College Press, London, 2014 (616 pages)

22. R. F. Eagerton, Physical Principles of Electron Microscopy: An Introduction to TEM, SEM and AEM, Springer, USA, Edition 2, 2016 (211 pages)
23. P. Villars, L. D. Calvert, Pearson's handbook of crystallographic data for intermetallic phases, American Society of Metals, 1986, Vol. 1-3 (3258 pages)
24. D. Wang, C. Duan, Y. Yu, X. Li, Z. Wang, Y. Liu, C. Liu, Co-regulation of anion-cation in transition metal high entropy oxide for outstanding OER electrocatalytic performance, J. Alloys Comp., 2023, Vol. 967, 171758 (8 pages)
25. Z. Wang, J. You, Y. Zhao, R. Yao, G. Liu, J. Lu, S. Zhao, Research progress on high entropy alloys and high entropy derivatives as OER catalysts, J. Environ. Chem. Eng., 2023, Vol. 11, 109080 (24 pages)
26. J. Baek, Md. D. Hossain, P. Mukherjee, J. Lee, K. T. Winther, J. Leem, Y. Jiang, W. C. Chueh, M. Bajdich, X. Zheng, Synergistic effects of mixing and strain in high entropy spinel oxides for oxygen evolution reaction, Nat. Commun., 2023, Vol. 14, 5936 (11 pages)